Investigation of helium-3 ion usage in radiography for patient position verification in particle therapy

Ilze Baumgarte[1], Kristaps Palskis[2], and Maurizio Vretenar[3]

[1]Riga Technical University
[2]Institute of Particle Physics and Accelerator Technologies, Riga Technical University
[3]CERN, Next Ion Medical Machine Study Collaboration

Abstract
The report follows an investigation of the potential of helium-3 ions as an alternative to helium-4 ions in radiographic imaging within the context of helium ion therapy. The primary object was to determine whether helium-3 can achieve comparable or superior image quality to helium-4 ions. Monte Carlo simulations were employed to model the particle paths through a variety of phantom setups. The simulated data were then processed using image reconstruction techniques - most-likely-path (MLP) algorithm with point-of-interest binning (PIB). Image quality was assessed through several key metrics, including contrast-to-noise ratio (CNR), spatial resolution, comparison with the theoretically expected image and low contrast resolution. The findings suggest that helium-3 ions have the potential to provide high-quality imaging in particle therapy, offering a viable alternative to helium-4.

Keywords
Ion radiography, Particle therapy, Helium therapy, Monte Carlo simulations, Geant4

1 Introduction

Particle therapy offers significant advantages over conventional X-ray therapy by delivering charged particles, such as protons or helium ions, that deposit most of their energy at a specific depth known as the Bragg peak. This precise energy deposition allows for greater control over targeting tumors while minimizing damage to surrounding healthy tissues. However, one of the main challenges in particle therapy is accurately localizing the Bragg peak within the body, which can be influenced by patient movement, anatomical changes, and uncertainties in the tissue's stopping power.

Ion radiography is an advanced imaging technique that uses charged particles to generate precise images, playing a critical role in particle therapy for cancer treatment and daily patient positioning. Unlike conventional X-ray imaging, particle radiography utilizes the treatment beam - often composed of protons or heavy ions - to acquire images that directly reflect the tissue's stopping power, thereby reducing uncertainties in treatment planning, particularly regarding the Bragg peak position. While Helium-4 ions have been increasingly explored for this purpose, the potential of helium-3 ions remain under-researched. Helium-3 offers possible advantages, including lower imaging dose requirements and the ability to be accelerated to imaging energies with less demanding accelerator conditions, such as those proposed by the CERN Next Ion Medical Machine Study (NIMMS) collaboration. This study investigates the feasibility of using helium-3 ions for radiography, focusing on the achievable image quality compared to helium-4 ions.

2 Methodology

2.1 Physical properties

2.1.1 Ion energies

Before further investigation, methodology behind the selection of ion energies for radiography is given. The constraints of the NIMMS synchrotron design, energies were chosen such that radiographic images could be achieved for phantom thicknesses of 16 and 32 cm. [1]

The NIMMS synchrotron is designed to accelerate helium-4 ions up to 220 MeV per nuclon. The design constraint sets the framework for determining the maximum kinetic energy for helium-3 ions. [1]

The rest mass energy of helium-4 ion was calculated using the relationship:

$$E_{rest,He4} = m_{He4} * c^2 \tag{1}$$

where m_{He4} is the rest mass of helium-4 nucleus and c is the speed of light.

Given the kinetic energy $E_{kin,He4}$ of helium-4 ions, the relativistic parameters - relativistic β and the Lorentz factor γ - were determined using the equations:

$$\gamma = \frac{E_{tot}}{E_{rest}} = \frac{E_{kin} + E_{rest}}{E_r est} \tag{2}$$

$$\beta = \sqrt{1 - \frac{1}{\gamma^2}} \tag{3}$$

With these parameters, the momentum p of helium-4 ions was calculated as:

$$p = \gamma * m_{He4} * \beta * c \tag{4}$$

Momentum value is essential for determining the magnetic rigidity $B\rho$ of the synchrotron, given by:

$$B\rho = \frac{p}{q} \tag{5}$$

where q is the charge of helium ion.

According to equation (5), design rigidity of NIMMS helium synchrotron is X T*m. This value was then used to calculate the maximum momentum that the synchrotron could impart to helium-3 ions, expressed as:

$$p_{He3} = B\rho * q_{He3} \tag{6}$$

considering the differences in charge and mass between helium-3 and helium-4.

Similarly, as with the helium-4 ions, the rest mass energy of helium-3 was calculated. Finally, the maximum kinetic energy $E_{kin,He3}$ that the synchrotron could provide to helium-3 ions was computed using:

$$E_{max} = (\gamma_{He3} - 1) * E_{rest,He3} \tag{7}$$

where γ_{He3} was derived from the maximum momentum and rest mass energy:

$$\gamma_{He3} = \sqrt{1 + (\frac{p_{He3}}{E_{rest,He3}})^2} \tag{8}$$

With the maximum kinetic energy of helium-3 determined, the Bethe-Bloch formula is applied to calculate the stopping power of helium ions in water, which is critical for determining the depth at which the Bragg peak occurs:

$$\frac{dE}{dx} = -\frac{4\pi z^2 e^4}{m_e c^2 \beta^2} * \frac{NZ}{A} * (\ln \frac{2 m_e c^2 \beta^2 \gamma^2 T_{max}}{I^2} - \beta^2) \tag{9}$$

Table 1: Energies and Depths for Helium-3 and Helium-4

	Helium-3		Helium-4	
Thickness of Phantom, cm	16	32	16	32
Energy, MeV/u	261	364	220	305

The Bethe-Bloch formula is used to calculate the energy loss per unit distance (MeV/cm) as helium ions travel through the water. A continuous slowing down approximation is employed. Starting with the maximum kinetic energy, the energy loss is iteratively calculated for each 0.01 cm step in depth, until the energy reaches zero. For the energy range studies, Bethe Bloch formula was used without any additional corrections.

The calculated depth at which helium-3 ions reach their Bragg peak provides a key parameter for comparing with helium-4 ions. The energy required for helium-4 ions to reach the same depth and achieve a Bragg peak was also calculated using the Bethe-Bloch formula. Although the synchrotron cannot accelerate helium-4 ions to such energy levels, this calculated energy allows for a direct comparison between helium-3 and helium-4 ions in the 32 cm phantom. This highlights the differences in energy requirements and performance between the two ion types for phantom thicknesses studied.

The same approach was used to determine helium-3 energy for 16 cm phantom, using helium-4 energy of 220 MeV per nuclon as reference depth.

2.1.2 Water-Equivalent-Path-Length (WEPL)

Water-Equivalent Path-Length (WEPL) is a key concept in particle radiography, converting the physical path length through any material into a equivalent water path that causes the same energy loss in a particle beam. [2] This relies on relative stopping power (RSP), which compares the material's stopping power to that of water. [3]

The WEPL lookup tables serve as a crucial intermediary between kinetic energy and WEPL values, translating the amount of energy a particle loses while traveling through a material into a WEPL. These tables are derived from stopping power calculations and relate specific ion energies to WEPL, which is then used to differentiate contrast in reconstructed images across various target materials. By calculating the energy loss as a particle passes through matter, the lookup table allows for precise mapping of kinetic energy to WEPL, enabling accurate image reconstructions in particle radiography.

2.1.3 Scattering calculations

2.1.3.1 Momentum-velocity function

To take into account the Multiple Coulomb Scattering (MCS) processes into the Most Likely Path (MLP) formalism, it is necessary to calculate certain parameters, such as the momentum-velocity relationship, related to ion energy. The momentum-velocity relationship for each ion energy was calculated using the momentum-velocity function:

$$\frac{1}{\beta^2(u)p^2(u)} = \frac{(E_u + E_{rest})^2 c^2}{(E(u) + 2E_{rest})^2 E^2(u)} \tag{10}$$

where u is depth. This function is essential for reconstructing images using the most-likely-path algorithm and is dependent on the initial ion energies. The calculations accounted for the kinetic energy's variation with depth, as determined by the Bethe-Bloch formula, ensuring accurate tracking of ion paths, which is vital for achieving high-resolution imaging.

As further step in the analysis, the calculated functions were approximated using a fifth-order polynomial. This approximation makes data manipulation easier. [4]

Table 2: Approximation Coefficients of Momentum-Velocity Function

	Helium-3	Helium-4
Energy, MeV/u	**261**	**220**
α_1	$5.13467719 * 10^{-7}$	3.94509135810^{-7}
α_2	$1.83027839 * 10^{-8}$	$1.39847713 * 10^{-8}$
α_3	$4.33309431 * 10^{-10}$	$3.32453972 * 10^{-10}$
α_4	$5.85636765 * 10^{-11}$	$4.42525018 * 10^{-11}$
α_5	$-3.12233562 * 10^{-12}$	$-2.34562166 * 10^{-12}$
α_6	$1.70244368 * 10^{-13}$	$1.28371217 * 10^{-13}$

2.1.3.2 Scattering integrals and matrices

To accurately describe scattering processes, scattering matrices were employed, based on the Gaussian approximation in the multiple Coulomb scattering (MCS) framework. These matrices, Σ_1 and Σ_2, capture the statistical relationships between lateral displacement t and angular deviation θ of ions at different depth points u_0, u_1, u_2. The matrix Σ_1 represents the scattering at the start of ion path, while Σ_2 characterizes the scattering near the end:

$$\Sigma_1 = \begin{bmatrix} \sigma_{t_1}^2 & \sigma_{t_1\theta_1}^2 \\ \sigma_{t_1\theta_1}^2 & \sigma_{\theta_1}^2 \end{bmatrix} \tag{11}$$

$$\Sigma_2 = \begin{bmatrix} \sigma_{t_2}^2 & \sigma_{t_2\theta_2}^2 \\ \sigma_{t_2\theta_2}^2 & \sigma_{\theta_2}^2 \end{bmatrix} \tag{12}$$

The scattering matrices incorporate integrals that account for energy loss and scattering throughout the proton's path. These integrals represent the accumulated variance and covariance of the proton's lateral displacement and angular deviation due to scattering between depth points. The variance for lateral displacement t and angular deviation θ at different depth intervals is calculated using the following integrals:

$$\sigma_{t_1}^2 = 4 * E_0^2 (1 + 0.038 \ln \frac{u_1 - u_0}{X_0})^2 * \int_{u_0}^{u_1} \frac{(u_1 - u)^2}{\beta^2(u) p^2(u)} \frac{du}{X_0} \tag{13}$$

$$\sigma_{\theta_1}^2 = 4 * E_0^2 (1 + 0.038 \ln \frac{u_1 - u_0}{X_0})^2 * \int_{u_0}^{u_1} \frac{1}{\beta^2(u) p^2(u)} \frac{du}{X_0} \tag{14}$$

$$\sigma_{t_1\theta_1}^2 = 4 * E_0^2 (1 + 0.038 \ln \frac{u_1 - u_0}{X_0})^2 * \int_{u_0}^{u_1} \frac{u_1 - u}{\beta^2(u) p^2(u)} \frac{du}{X_0} \tag{15}$$

$$\sigma_{t_2}^2 = E_0^2 (1 + 0.038 \ln \frac{u_2 - u_1}{X_0})^2 * \int_{u_1}^{u_2} \frac{(u_2 - u)^2}{\beta^2(u) p^2(0)} \frac{du}{X_0} \tag{16}$$

$$\sigma_{\theta_2}^2 = 4 * E_0^2 (1 + 0.038 \ln \frac{u_2 - u_1}{X_0})^2 * \int_{u_1}^{u_2} \frac{1}{\beta^2(u) p^2(u)} \frac{du}{X_0} \tag{17}$$

$$\sigma_{t_2\theta_2}^2 = 4 * E_0^2 (1 + 0.038 \ln \frac{u_2 - u_1}{X_0})^2 * \int_{u_1}^{u_2} \frac{u_2 - u}{\beta^2(u) p^2(u)} \frac{du}{X_0} \tag{18}$$

where X_0 is the radiation length, $\beta(u)$ is the particle's velocity relative to the speed of light, and $p(u)$ is the momentum at depth u. Approximated fifth-order polynomials from the momentum-velocity function were employed in these integrals, allowing for more efficient calculations and accurate modeling of ion trajectories. The radiation length in this scenario is 36.1 cm, assuming that the scattering object consists of water. Also, the u values were chosen so that the MLP images were formed in the middle of the phantom, with values u_0, u_1 and u_2 being (0, 8, 16) cm and (0, 16, 32) cm.

Additionally, geometric matrices were used to transform the proton's spatial coordinates through different depth intervals. These matrices R_0 and R_1 describe the positional and angular adjustments during the ion's travel. [4]

$$R_0 = \begin{bmatrix} 1 & (u_1 - u_0) \\ 0 & 1 \end{bmatrix} \tag{19}$$

$$R_1 = \begin{bmatrix} 1 & (u_2 - u_1) \\ 0 & 1 \end{bmatrix} \tag{20}$$

2.2 Monte Carlo simulations

In this study, Monte Carlo simulations were employed to model helium ion paths through a series of phantoms designed for spatial and contrast resolution investigation. The simulations were conducted in the Geant4 environment (version 11.2.1), providing a detailed analysis of particle interactions with various materials. All simulations were executed using the high-performance computing (HPC) resources of Riga Technical University, ensuring efficient processing and accurate modeling of the ion trajectories across both spatial and low contrast phantoms.

2.2.1 GEANT4 environment

2.2.1.1 Physics list

The QGSP BIC HP EM4 physics list - self-customed for required simulation setup - provides a highly detailed and flexible framework for simulating particle interactions across a wide range of energies and processes. Key features include:

- **Electromagnetic physics** with Electromagnetic Option4 model, offering enhanced precision for low-energy particle interactions. It includes models for ionization, bremsstrahlung, Compton scattering, and photoelectric effect, along with high-precision electron and gamma processes. [5]
- **Hadronic physics** combines the Quark-Gluon String Model (QGSP) for high-energy interactions and Binary Cascade Model (BIC) for low-to-intermediate-energy hadronic processes. [6], [7]
- **Neutron physics** is modeled with the High Precision (HP) neutron model, providing simulations for low-energy neutron behavior - elastic and inelastic scattering, capture, and fission. [8]
- **Ion physics** relies on BIC model to simulate ion-nucleus interactions and energy loss, relevant for radiation and medical applications. [6]

2.2.1.2 Step and range limits

The step limit defines the length of the step after which a particle in the simulation must interact with its environment. A step limit of 1 mm was selected for the simulation, based on literature review. [9]

The range cut determines the minimum energy - minimum remaining range - to which the particle is tracked. The range cut in given simulation was set to 0.5 mm. [22]

2.2.1.3 Particle beam

As source position a uniform square field with dimensions of 10x10 cm is used to simulate the particle's beam starting configuration.

The beams initial velocity direction in similar studies is typically assumed to be parallel, but for more realistic simulation, in our investigation the beam divergence was introduced. The divergence is modeled by defining the direction of the particle momentum in spherical coordinates:

$$p_x = \sin(\theta) * \cos(\phi) \tag{21}$$

$$p_y = \sin(\theta) * sin(\phi) \tag{22}$$

$$p_z = \cos(\theta) \tag{23}$$

Here θ is the polar angle and ϕ is the azimuthal angle. To introduce beam divergence in this setup, polar angle was sampled from a normal distribution between $(0; 2\pi)$, while azimuthal angle - sampled from a normal distribution with a standard deviation of 3 mrad, value based on literature review [11] As a result, the momentum vector is (p_x, p_y, p_z).

The beam's energy spread is introduced based on the assumption of a momentum spread $\Delta p/p = 0.1\%$. [12] However, in Geant4 the energy spread is implemented instead of directly using momentum spread. The process to determine the energy spread involves:

– calculating momentum from the particle's kinetic energy;
– computing the range of momentum by applying the spread;
– converting the resulting momentum values back into kinetic energy
– subtracting these energies from the nominal energy to define the energy spread $\Delta E/E$.

For the same momentum spread assumption, it showed that energy spread is slightly affected by the initial kinetic energy of the ion. Thus a constant value of 0.2 % was assumed, based on before mentioned calculations.

2.2.1.4 Detector

In the idealized detector setup, the simulation defines the detector as a gaseous - air - volume, with the target - phantom - positioned centrally. The gas acts as the detector medium, capturing particles that pass through it. The air layer have a thickness of 1 mm.

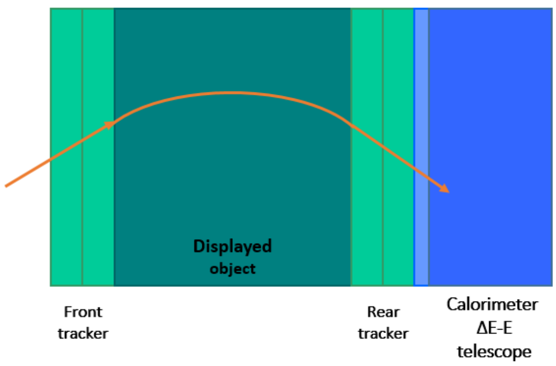

Figure 1: Conceptual Scheme of Detector and Phantom Setup

2.2.1.5 ΔE-E filter

In helium radiography one of the major challenges is dealing with the fragmentation of helium ions as they interact with the target material. These fragments often have energies that are very similar to the primary helium ions, making it difficult to distinguish between them.

To address this problem, the ΔE-E filter was implemented in simulation setup. This filter consists of two detectors a thin ΔE detector to measure the energy loss by the particle as it slows down, and a thicker E detector to measure the total remaining energy of the particle. Since different particles have distinct energy loss characteristics based on their mass and charge, this method allows for the separation of primary helium ions from fragments like helium isotope ions and heavy particles. [13]

In Geant4, the ΔE was implemented as a 1 mm thick layer of polystyrene placed to measure the energy loss. Polystyrene was chosen due to low atomic number and well-defined stopping power. Low-Z materials allows charged particles to loose a predictable, moderate amount of energy as they pass through the medium. [13]

2.2.1.6 Data registration and filtration

Data registration is performed as particles cross the front and rear detector volumes, ensuring a complete record of particle interactions. The input and output parameters - such as position (x, y), angles (x, y), energy and time - are captured and linked via track ID.

Specifically for the ΔE-E filter, the energy deposition is recorded to identify the energy loss of particles as they traverse the polystyrene layer.

In the first filtration step that is employed within Geant4 code itself, secondary particles - gamma rays, electrons, positrons, neutrinos and anti-neutrinos - are filtered out. This ensures that only relevant particles, such as primary ions and their significant fragments, are processed.

2.2.1.7 Phantom geometry

Two distinct phantom setups were implemented in the simulation to investigate both spatial and low contrast resolution.

To assess spatial resolution, a phantom containing a high-contrast material was used. This phantom consisted of a 2x2x2 cm aluminium cube positioned at the center, offering a significant contrast due to the high density and RSP of aluminium ($RSP_{Al} \approx 2.41$)

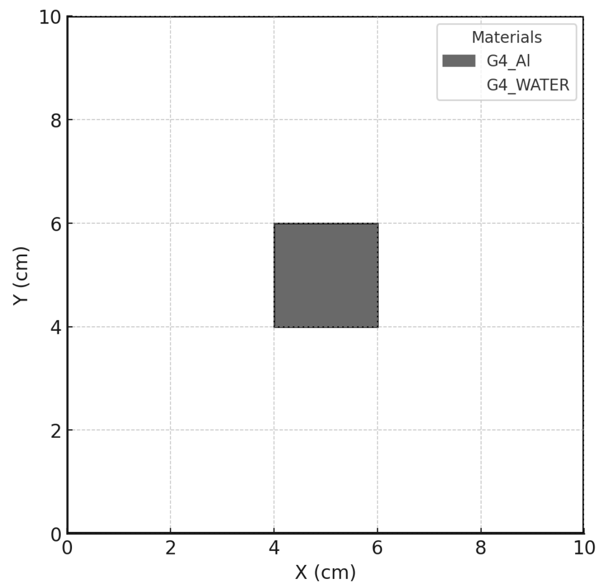

Figure 2: Phantom Geometry for High Contrast Evaluation

For the low contrast resolution analysis, a phantom with 36 embedded cylinders was used, each column representing a different level of contrast relative to water. The materials for these cylinders were selected based on their RSP values, ensuring a gradual and controlled change in contrast resolution. [14] Material properties were researched using the Geant4 material database. [15]

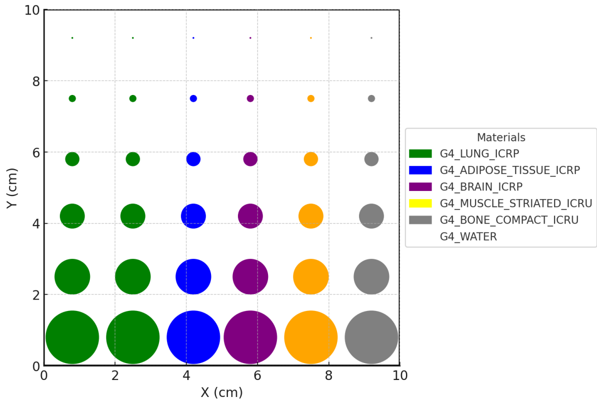

Figure 3: Phantom Geometry for Low Contrast Evaluation

Material	Z	A	rho	I	RSP	Contrast difference
G4_LUNG_ICRP	7.14	14.18	0.026	75.3	0.26	-1 %
						-2.5 %
G4_ADIPOSE_TISSUE_ICRP	5.91	11.69	0.92	63.2	0.95	-0.5 %
G4_BRAIN_ICRP	7.06	14.03	1.03	73.3	1.03	+0.5 %
G4_MUSCLE_STRIATED_ICRU	7.15	14.21	1.04	74.7	1.04	+1 %
G4_BONE_COMPACT_ICRU	9.25	18.50	1.85	91.9	1.79	+2.5 %

Table 3: Table of Materials and Properties

The thickness of each cylinder for different materials was calculated using:

$$x = \frac{WEPL_{material} * (1 + contrast) - WEPL_{water}}{RSP_{material} - 1} \tag{24}$$

This formula takes into account the RSP of the material and the contrast level compared to water.

Material	Thickness (16 cm), cm	Thickness (32 cm), cm
G4_LUNG_ICRP	0.2	0.4
	0.5	1.1
G4_ADIPOSE_TISSUE_ICRP	1.5	3.1
G4_BRAIN_ICRP	3.2	6.4
G4_MUSCLE_STRIATED_ICRU	4.5	9.0
G4_BONE_COMPACT_ICRU	0.5	1.1

Table 4: Cylinder Thicknesses Based on Contrast

2.3 Image reconstruction

After the simulations, all data were used as inputs for an image reconstruction algorithm to generate the corresponding images. This step is crucial in translating the raw data into meaningful visual representations of the ion interactions within the medium. Both the image reconstruction and subsequent image analysis were conducted within a Python environment, utilizing its robust libraries and tools to ensure accurate and efficient processing of the simulation data.

2.3.1 Most-likely-path algorithm

The MLP algorithm calculates the path of a charged particle through a medium using Bayesian statistics and a Gaussian approximation of multiple Coulumb scattering (MCS). The method estimates the particle's position and direction at any given depth by maximizing the likehood of the observed entry and exit point.

The position of a particle was estimated using covariance matrices Σ_1 and Σ_2 at the entry and exit points, and R_0 and R_1 geometric matrices accounting for the geometry of the path at different depths:

$$x_{MLP} = (\Sigma_1^{-1} + R_1^T \Sigma_2^{-1} R_1)^{-1} (\Sigma_1^{-1} R_0 x_0 + R_1^T \Sigma_2^{-1} x_2) \tag{25}$$

$$y_{MLP} = (\Sigma_1^{-1} + R_1^T \Sigma_2^{-1} R_1)^{-1} (\Sigma_1^{-1} R_0 y_0 + R_1^T \Sigma_2^{-1} y_2) \tag{26}$$

The formalism models the scattering effects by using a scattering matrix based on the ion's position and energy loss, providing a smooth MLP path for reconstruction. [4] Using MLP formalism, image reconstruction can be done at any depth within the phantom, thus various binning approaches are employed. Within this study, point-of-interest binning (PIB) was used, setting the reconstruction depth at the position corresponding to the middle of phantom.

2.3.2 Data filtering

2.3.2.1 Energy filter

The energy filter was implemented in two ways - for simple geometries as for high contrast - via a Gaussian function fit -, while for complex geometries - filtering was done individually for each pixel.

The energy filter for simple phantom setup uses a Gaussian fit to the most frequent energy value in the distribution. By fitting a Gaussian curve to the energy histogram, the filter applies a 3σ rule, excluding particles with energies outside three standard deviations from the mean:

$$\mu_E - 3\sigma_E \leq E \leq \mu_E + 3\sigma_E \tag{27}$$

where μ_E is the mean energy, and σ_E is the standard deviation of the energy distribution. Additionally, due to the presence of a high-contrast material - aluminum - in the phantom, a double Gaussian fit was applied to account for the two distinct energy loss profiles - one for the regions passing through the aluminum and another for the rest of the phantom medium.

For more complex phantoms with varying materials, such as the low contrast phantom, pixel-wise filtration is applied. Here, each pixel has a unique energy distribution, so a local mode is computed for each pixel. [16] Energy values are retained if they fall within 25 % of the mode for that pixel:

$$0.75 * mode_E(p) \leq E(p) \leq 1.25 * mode_E(p) \tag{28}$$

followed by another 3σ filter applied to the energy distribution within each pixel. The mean and standard deviation are calculated directly from the array.

2.3.2.2 Count filter

The count filter removes events where multiple particles are detected at the exit for a single entry particle. It ensures a 1-to-1 correspondence between the detected input and output particles. In case, if no particles are detected, these events are also discarded.

2.3.2.3 Relative angle filter

Relative angle filtration is important as it helps remove particles whose angular deviations deviate significantly from the expected path, therefore removing events due to large angle MCS. This step ensures that only particles following predictable and accurate trajectories contribute to the final image, reducing noise and improving the spatial resolution.

The relative angle filter calculates the angular deviation of particles between their entry and exit points. For each particle, the relative angles $\Delta\theta_X$ and $\Delta\theta_Y$ are computed as:

$$\Delta\theta_X = \theta_{X_{out}} - \theta_{X_{in}} \tag{29}$$

$$\Delta\theta_Y = \theta_{Y_{out}} - \theta_{Y_{in}} \tag{30}$$

Similar to the energy filter, a 3σ filter is applied to discard particles whose angular deviations fall outside three standard deviations of the distribution:

$$\mu_{\Delta\theta} - 3\sigma_{\Delta\theta} <= \Delta\theta <= \mu_{\Delta\theta} + 3\sigma_{\Delta\theta} \tag{31}$$

2.3.2.4 ΔE-E filter

To test the effectiveness of additional ΔE-E filter, it was implemented as an additional step before energy filtration. Parameters of deposition energy $E_{dep/low}$ and $E_{dep/high}$, are computed based on the expected stopping power of the detector material - polystyrene. These bounds are calculated using interpolation derived from the Bethe-Bloch formula. Interpolated bounds are based on the particle energy-stopping power relationship and are designed to cover the region with the highest particle density, ensuring only the particles with appropriate energy deposition values are included.

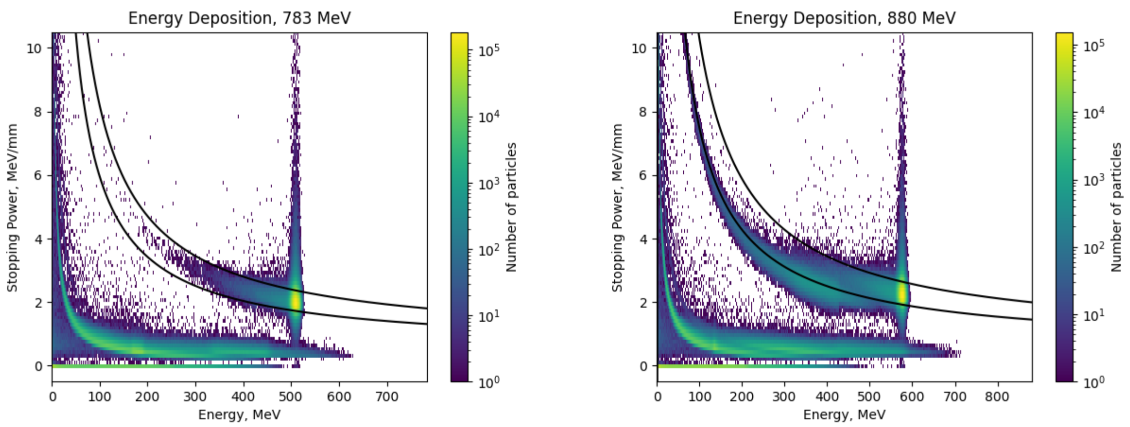

Figure 4: Stopping Power Margins Used for ΔE-E Filter Implementation. In the Left - Helium-3, in the Right - Helium-4

The actual energy deposition E_{dep} is compared against the calculated bounds. Particles are retained only if:

$$E_{dep/low} \leq E_{dep} \leq E_{dep/high} \tag{32}$$

2.3.3 Pixel binning

In the image reconstruction process, pixel binning was employed to organize the ion data into discrete pixel units for analysis. A resolution of 0.2 mm per pixel was used to ensure high spatial detail. The ion trajectories, calculated using the most-likely-path (MLP) method, were traced from entry to exit, and the lateral positions at the reconstruction depth - middle of phantoms - were used to assign them to corresponding pixel bins. The binning process involved defining both the pixel edges and centers across the x and y axes, with special attention given to ions passing through key regions, such as the aluminum cube. This binning ensured that the data could be accurately analyzed and compared across different regions of interest in the phantom. [17]

2.4 Image analysis

The quality of the reconstructed images was assessed using several parameters tailored to both spatial and low contrast phantoms. For high resolution phantom setup, the modulation transfer function (MTF), contrast-to-noise ratio (CNR), and the difference between the theoretical and experimental images were used to evaluate the precision of images. For low contrast resolution, the analysis focused on both quantitative and qualitative object visual definition, along with comparison between theoretical and experimental images.

2.4.1 Spatial resolution

The MTF is a key metric for assessing spatial resolution, quantifying how well an imaging system can reproduce varying levels of detail in terms of spatial frequency. The MTF is defined as normalized Fourier transform of the system's point spread function (PSF), given by:

$$MTF(f) = \frac{|FPSF(x)|}{|FPSF(0)|} \tag{33}$$

The MTF was implemented in the code to analyze energy profiles at different spatial frequencies. The calculation of MTF involves extracting central horizontal and vertical profiles of the image of phantom with high contrast material, applying Fourier transformation, and determining the 50 % and 10 % MTF points through interpolation. The spatial frequency at these points provides insight into system's ability to resolve fine details. [18]

2.4.2 Contrast-to-noise ratio

To obtain the dose values for CNR evaluation, several simulations were performed using different particle counts. The simulations were run with 10^7, $5 * 10^6$, 10^6, and $5 * 10^5$ ions, allowing for a range of dose values to be assessed at varying particle intensities. These simulated doses were then used to evaluate the relationship between contrast-to-noise ratio (CNR) and dose for both helium-3 and helium-4 ions.

The CNR is a measure used to quantify the ability of an imaging system to distinguish between two objects of varying contrast levels. Mathematically, CNR is expressed as:

$$CNR = \frac{|\mu_1 - \mu_2|}{\sqrt{\sigma_1^2 + \sigma_2^2}} \tag{34}$$

where μ_1 and μ_2 are the mean intensities of two regions of interest, and σ_1 and σ_2 are their respective standard deviations. [19] The chosen regions for CNR evaluation were aluminum and water.

2.4.3 Contrast analysis

In evaluating the low contrast phantom images, the process was carried out in several steps. First, the visibility of each cylinder was analyzed by comparing their contrast levels at varying energies. This allowed for a qualitative assessment of how well each cylinder could be visually distinguished from the background, depending on the energy range and contrast properties.

2.4.4 Comparison of theoretical and reconstructed images

In both the spatial and low contrast phantom analyses, the difference between the theoretical and experimental images was calculated to assess the accuracy of the image reconstruction. The theoretical image was generated by calculating the Water Equivalent Path Length (WEPL) for each material. For the spatial phantom, the theoretical image was based on the WEPL of water for the background and aluminum for the cube, with specific relative stopping power (RSP) values derived for aluminum:

$$WEPL_{Al} = WEPL_{wat} - 2 + 2 * RSP_{Al} \tag{35}$$

The cube was positioned at the center, and its dimensions were converted into pixel space. For the

Contrast, %	WEPL, 16 cm	WEPL, 32 cm
-2.5%	15.6	31.2
-1%	15.84	31.68
-0.5%	15.92	31.84
+0.5%	16.08	32.16
+1%	16.16	32.32
+2.5%	16.4	32.8

Table 5: Theoretical WEPL values for low-contrast phantom

low contrast phantom, a similar approach was used, with WEPL values assigned for different contrast differences.

3 Results

3.0.1 High contrast evaluation

Visually, the images generated from both helium-3 and helium-4 ions for the 16 cm and 32 cm phantoms appear very similar, making it difficult to immediately discern which ion provides better image quality.

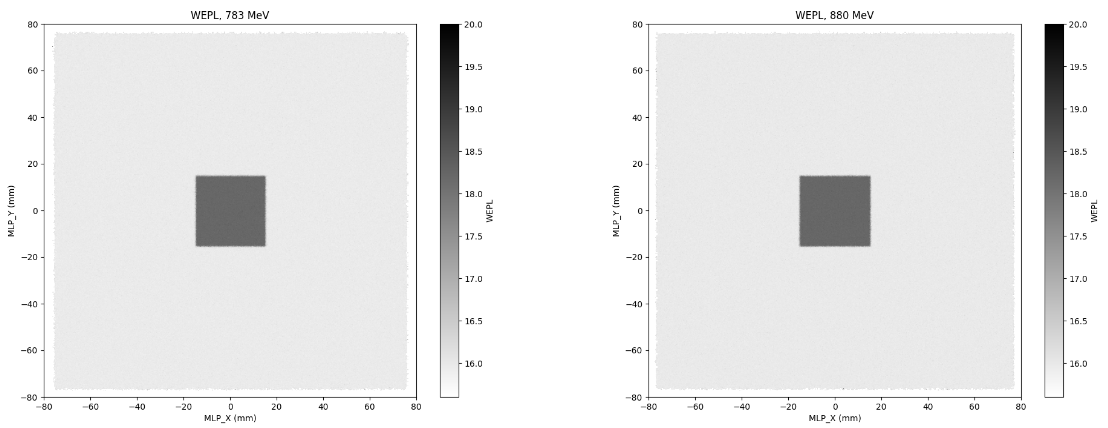

Figure 5: Reconstructed Images of 16 cm Phantoms. Left - Helium-3, Right - Helium-4

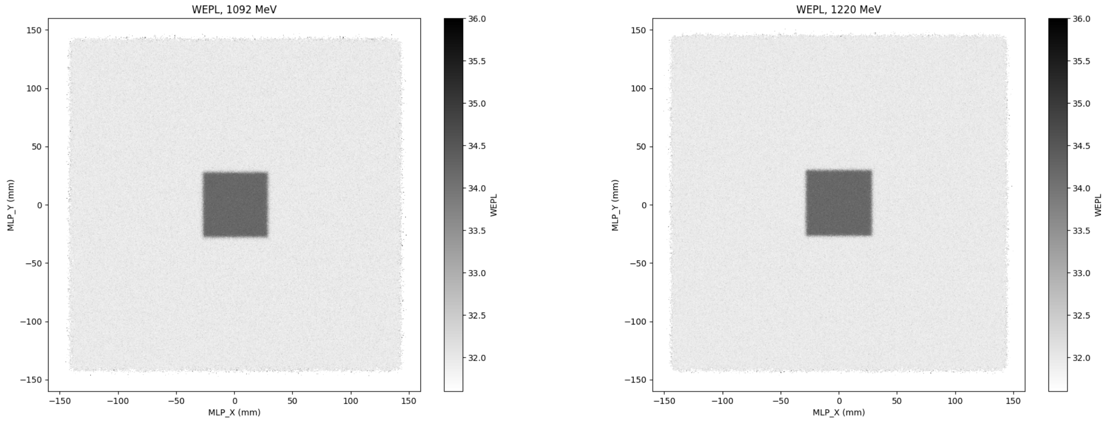

Figure 6: Reconstructed Images of 32 cm Phantoms. Left - Helium-3, Right - Helium-4

Both ion types produce well-defined contrast between the central square and surrounding area with consistent shading, suggesting minimal visual differences. While the images appear similar, the quantitative evaluation of spatial resolution and contrast-to-noise ratio (CNR) from subsequent MTF and CNR analyses will provide more precise insights into which ion performs better.

3.0.1.1 Spatial resolution

The MTF for both helium-3 and helium-4 ions at different energies and phantom sizes are visually represented in figures 6 and 7. The profiles highlight how well each ion maintains image quality at various spatial frequencies.

The MTF profiles for the 16 cm phantom show that helium-4 achieves slightly better performance than helium-3 in terms of spatial frequency. At 10 % level, helium-4 retains spatial frequency of 2.099 cycles/mm, while helium-3 only reaches 1.995 cycle/mm. This difference indicates that helium-4 provides slightly better spatial resolution. The trend is similar at the 50 % MTF level, where helium-4 reaches 1.019 cycles/mm, outperforming helium-3 at 0.971 cycles/mm. Thus, helium-4 demonstrates superior spatial resolution for the 16 cm phantom, where higher spatial frequencies are better preserved.

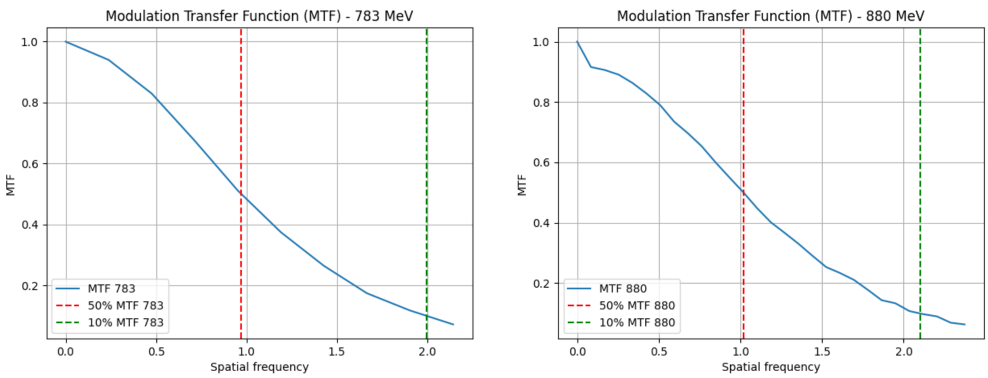

Figure 7: MTF for helium-3 and helium-4 ions in 16 cm depth

For the 32 cm phantom, however, helium-3 outperforms helium-4 in preserving spatial frequencies. At the 10 % MTF level, helium-3 retains a frequency of 1.093 cycles/mm, compared to 0.977

cycles/mm for helium-4. Similarly, at the 50 % MTF level, helium-3 maintains 0.431 cycles/mm, surpassing helium-4 at 0.398 cycles/mm.

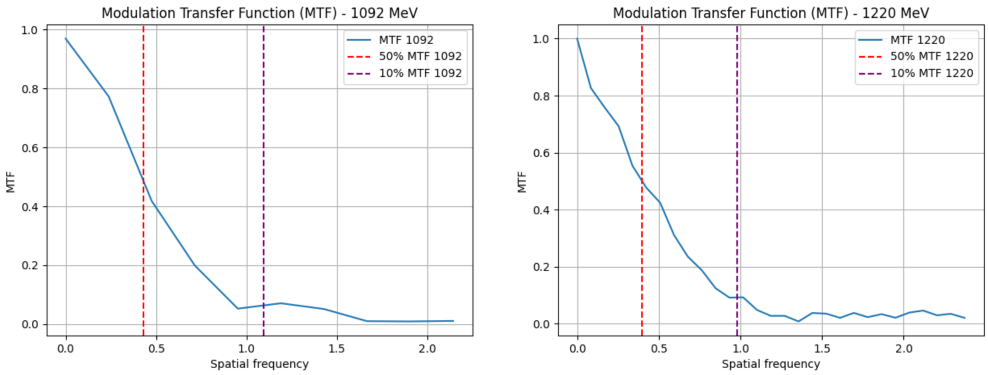

Figure 8: MTF for helium-3 and helium-4 in 32 cm depth

Despite the observed differences, the MTF values for both ions are quite close, indicating that both helium-3 and helium-4 provide comparable spatial resolution in the experimental setup, with only slight variations depending on phantom size and energies.

3.0.1.2 Contrast and noise

For the 32 cm phantom, as the dose increases, the CNR improves steadily for both ions. Helium-4 shows slightly better CNR values than helium-3, indicating that helium-4 provides a superior contrast differentiation at higher dose. At lower dose, however, the performance of both ions is more comparable. The higher CNR values for helium-4 suggest better contrast visibility for larger phantoms when using helium-4 at higher energy. Therefore to achieve the same level of CNR, helium-3 requires higher imaging dose compared to helium-4.

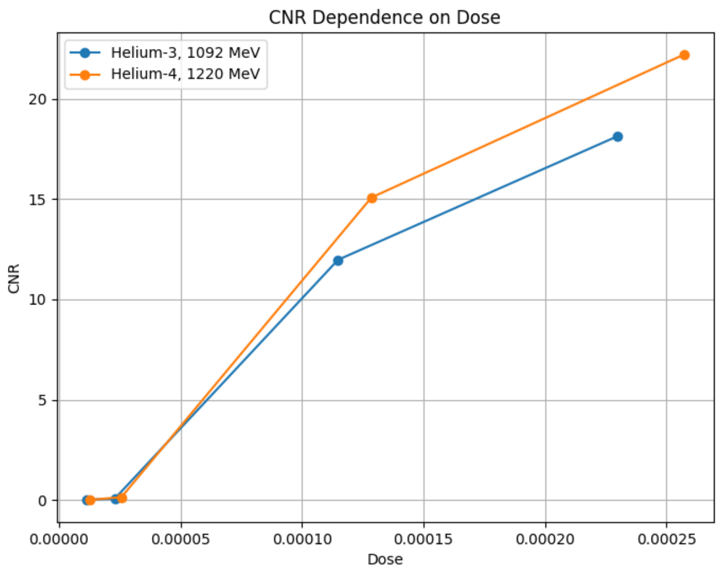

Figure 9: CNR and Dose Relationship for Helium-3 and Helium-4 at 32 cm Depth

For the 16 cm phantom, the CNR values rise sharply with increasing dose for both helium-3 and helium-4, especially at higher doses. This indicates that helium-3 provides better contrast resolution for smaller objects, where high contrast is required at lower doses. In a 16 cm phantom, a higher dose is required to achieve the same CNR level for helium-4.

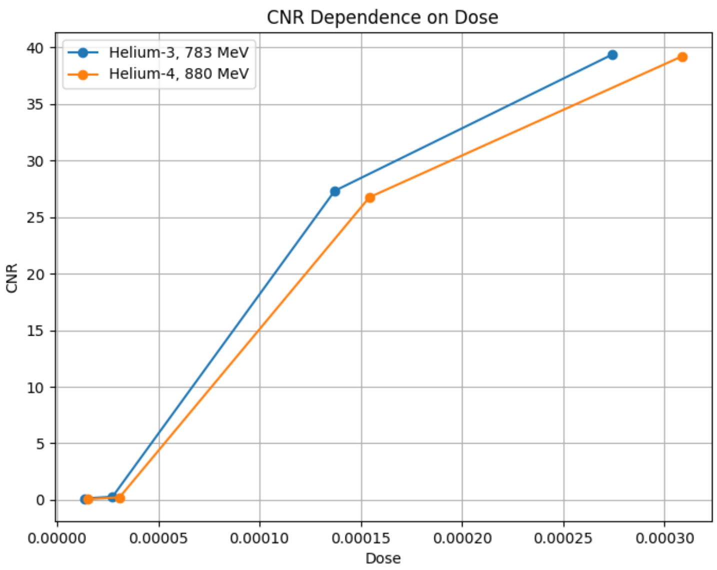

Figure 10: CNR and dose relationship for helium-3 and helium-4 at 16 cm depth

3.1 Low contrast evaluation

In the low-contrast evaluation, a noticeable difference emerges between the helium-3 and helium-4 ions, particularly at the depth of 16 cm. The WEPL image of helium-4 at 880 MeV appears visibly blurrier compared to helium-3 at 783 MeV, with the boundaries of the contrast cylinders being less distinct.

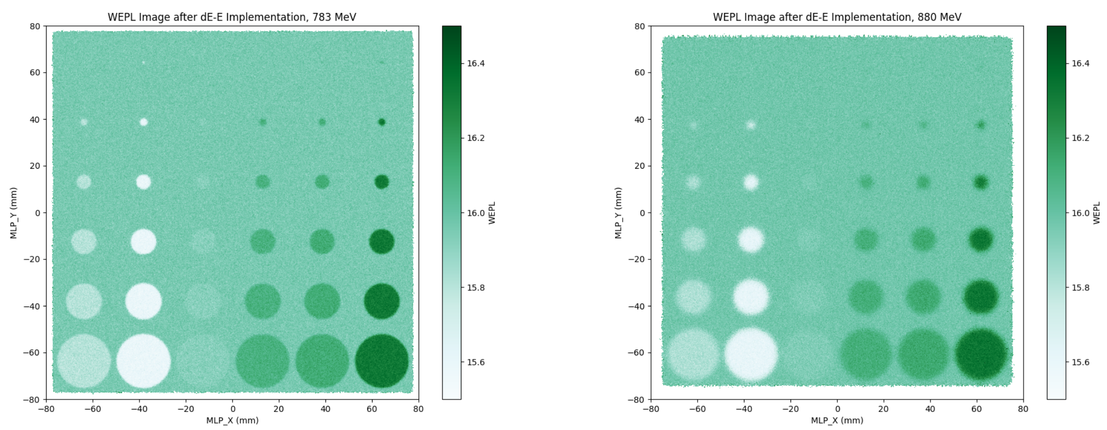

Figure 11: Reconstructed Images at 16 cm Depth. Left - Helium-3, Right - Helium-4

At greater depths - 32 cm phantom -, both ions perform similarly at higher energies, with helium-3 at 1092 MeV and helium-4 at 1220 MeV showing comparable contrast resolution.

In the low contrast analysis, all contrasts were visible for both helium-3 and helium-4, but the number of detectable cylinders varied between the two ions, especially for smaller contrast differences and finer diameters.

Helium-3 consistently detected a larger number of cylinders across various contrast levels, particularly at smaller contrast differences like 0.5 %. This indicates that helium-3 is better at resolving fine details, allowing more structures with smaller contrasts to be clearly visible, which is important for distinguishing subtle features in low contrast imaging.

Table 6: Visible Cylinders in 16 cm Phantom, 783 MeV

Diameter / Contrast	**He-3, 783 MeV**					
	1.5 cm	**1.0 cm**	**0.7 cm**	**0.4 cm**	**0.2 cm**	**0.05 cm**
+2.5%	+	+	+	+	+	+
+1%	+	+	+	+	+	+
+0.5%	+	+	+	+	+	-
-0.5%	+	+	+	+	+	-
-1%	+	+	+	+	+	-
-2.5%	+	+	+	+	+	+

Table 7: Visible Cylinders in 32 cm Phantom, 1092 MeV

Diameter / Contrast	**He-3, 1092 MeV**					
	1.5 cm	**1.0 cm**	**0.7 cm**	**0.4 cm**	**0.2 cm**	**0.05 cm**
+2.5%	+	+	+	+	+	-
+1%	+	+	+	+	+	-
+0.5%	+	+	+	+	+	-
-0.5%	+	+	+	+	-	-
-1%	+	+	+	+	+	-
-2.5%	+	+	+	+	+	+

Table 8: Visible Cylinders in 16 cm Phantom, 880 MeV

Diameter / Contrast	**He-4, 880 MeV**					
	1.5 cm	**1.0 cm**	**0.7 cm**	**0.4 cm**	**0.2 cm**	**0.05 cm**
+2.5%	+	+	+	+	+	+
+1%	+	+	+	+	+	-
+0.5%	+	+	+	+	+	-
-0.5%	+	+	+	+	+	-
-1%	+	+	+	+	+	-
-2.5%	+	+	+	+	+	+

Table 9: Visible Cylinders in 32 cm Phantom, 1220 MeV

Diameter / Contrast	He-4, 1220 MeV					
	1.5 cm	**1.0 cm**	**0.7 cm**	**0.4 cm**	**0.2 cm**	**0.05 cm**
+2.5%	+	+	+	+	+	-
+1%	+	+	+	+	+	-
+0.5%	+	+	+	+	+	-
-0.5%	+	+	+	-	-	-
-1%	+	+	+	+	+	-
-2.5%	+	+	+	+	+	-

Helium-4, while capable of detecting all contrast levels, showed limitations in the number of objects it could resolve, especially at smaller contrast differences. Although helium-4 performed well throughout various contrast levels, it resolved fewer cylinders when the contrast was minimal, highlighting its reduced resolution to fine details compared to helium-3.

3.2 WEPL accuracy

For the 16 cm phantom, the histogram show that the majority of the pixel differences are within 1-2 %. However, helium-4 demonstrates a tighter distribution of percentage difference, with fewer extreme values, suggesting that helium-4 produces a slightly more accurate image compared to helium-3 at this depth. The spatial distribution maps also confirm this, showing a more uniform spread of helium-4.

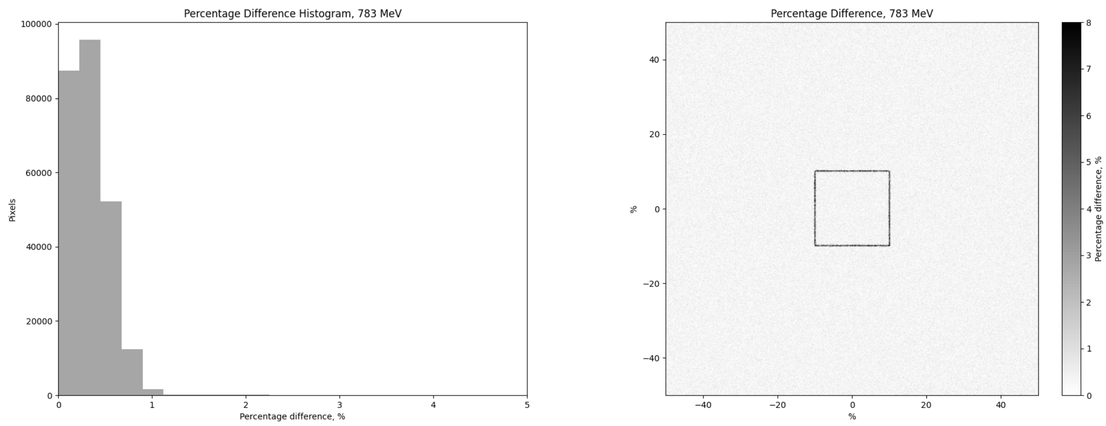

Figure 12: Comparison Between High Contrast Theoretical and Experimental Image, Helium-3

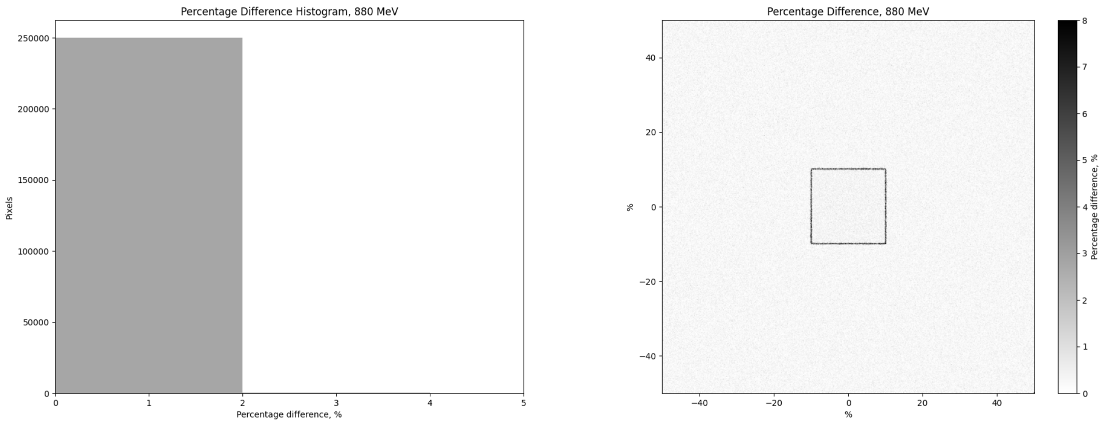

Figure 13: Comparison Between High Contrast Theoretical and Experimental Image, Helium-4

For the 32 cm phantom, both ions again show small percentage differences, with most pixels within 1-2 % range. However, in this larger phantom setup, helium-3 has a more concentrated distribution of differences compared to helium-4, indicating that helium-3 provides a more accurate reconstruction for larger depths. The most pronounced difference is observed at the edges of the object due to the ion scattering properties.

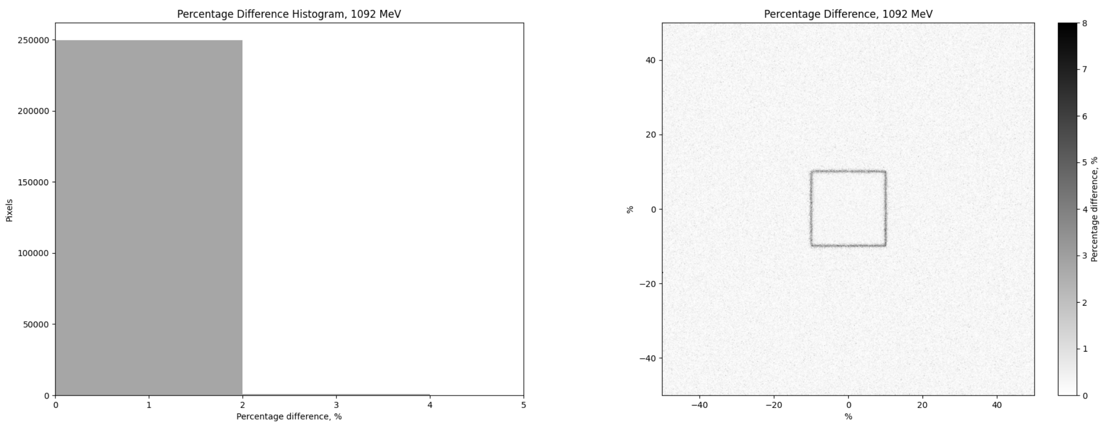

Figure 14: Comparison Between High Contrast Theoretical and Experimental Image, Helium-3

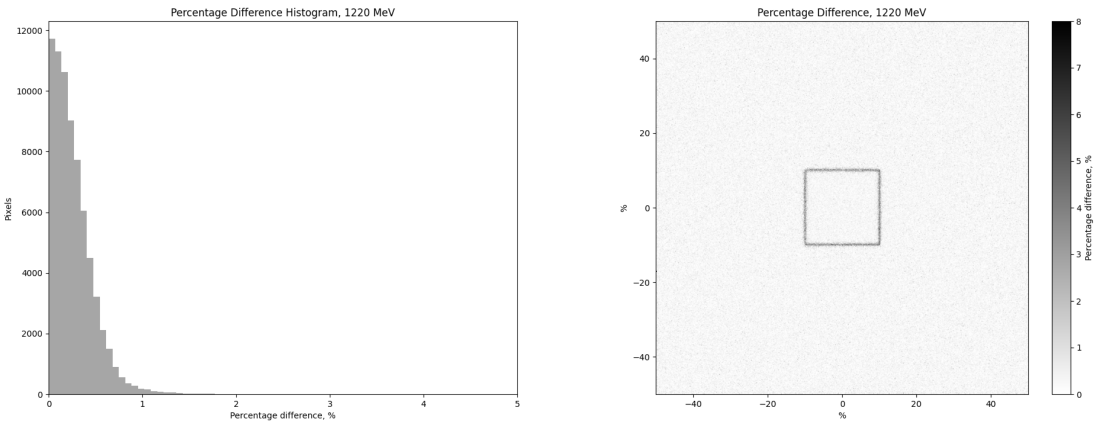

Figure 15: Comparison Between High Contrast Theoretical and Experimental Image, Helium-4

For both ions in, in the low contrast phantom the majority of pixels showed a small difference, concentrated below 1 %.

Helium-3 across all energy levels, demonstrated a tighter distribution of differences, where the variance remained low. The visual representation of colormaps confirms that helium-3 resulted in a more uniform image reconstruction, with fewer large deviations from the theoretical model, highlighting its accuracy in resolving low contrast features.

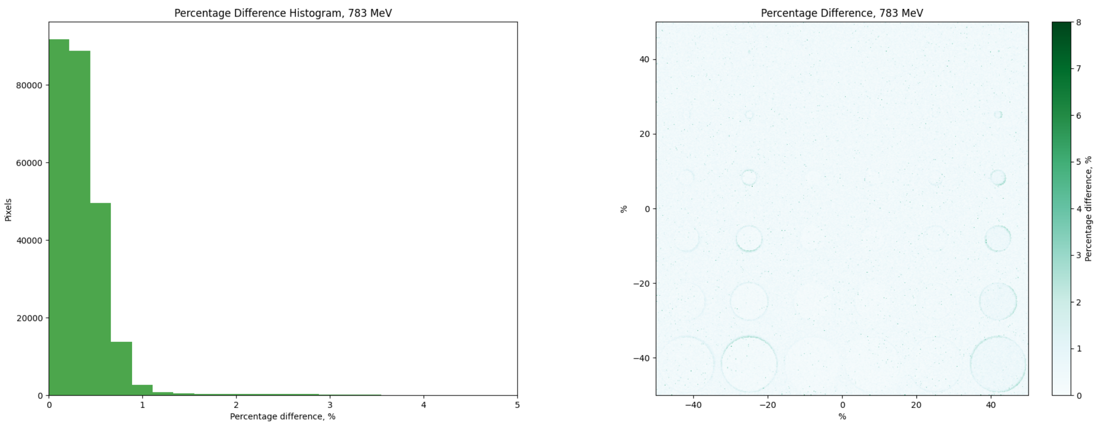

Figure 16: Comparison Between Low Contrast Theoretical and Experimental Image, Helium-3

Helium-4, while still showing a majority of pixels with a small difference, exhibited slightly higher deviations. This suggests that helium-4 introduces more variations in image reconstruction when dealing with low contrast objects, especially at bigger depths, though the overall performance remains strong.

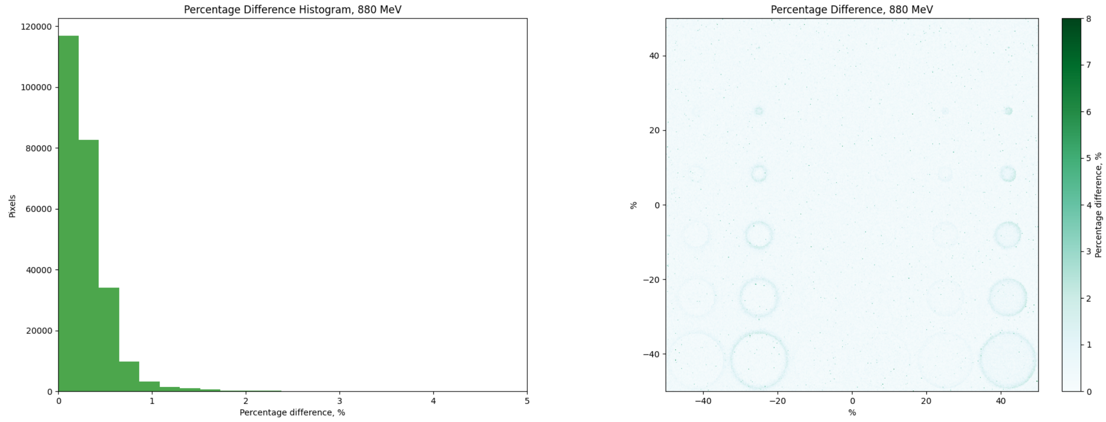

Figure 17: Comparison Between High Contrast Theoretical and Experimental Image, Helium-4

3.3 Rejection rates

For both the high and low contrast phantoms results suggest that helium-4, particularly at higher energies has higher data filtering rejections, suggesting that helium-4 ions undergo more physical interactions that are not relevant for radiographic reconstruction, thus requiring more stringent filtering to maintain image quality. The need for increased rejection rates may indicate that helium-4 interacts more with the phantom material, generating more scattered particles, including helium-3 fragments.

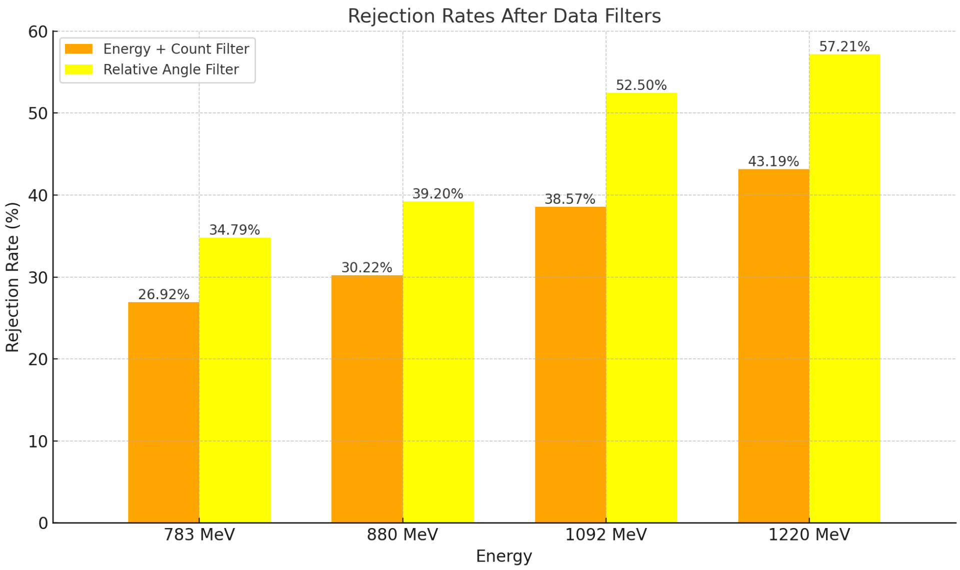

Figure 18: Rejection Rates for all Ion Energies after Filtering

However, even though helium-3 consistently shows lower rejection rates, the rates for both ions remain relatively high. This signals the persistent challenges in dealing with ion fragmentation, which affects the imaging process by generating secondary particles that require rigorous filtering.

3.4 ΔE-E filter

Upon reviewing the energy deposition plots for Helium-3 and Helium-4 across different energies, the ΔE-E filter demonstrates its effectiveness in reducing fragmentation and sharpening the energy profiles.

Helium-4 generally shows slightly broader peaks in the pre-filter profiles compared to helium-3 at similar energies. However, after filtering, both ions present well-defined, narrow energy peaks, indicating that the filter works efficiently for both ion types.

Helium-4 appears to have more pronounced fragmentation in the lower energy region compared to helium-3. The ΔE-E filter effectively reduces this fragmentation, but the difference in noise levels is more significant for helium-4.

Both ions benefit from the filtering, with sharp, clean Gaussian fits in the post-filter histograms.

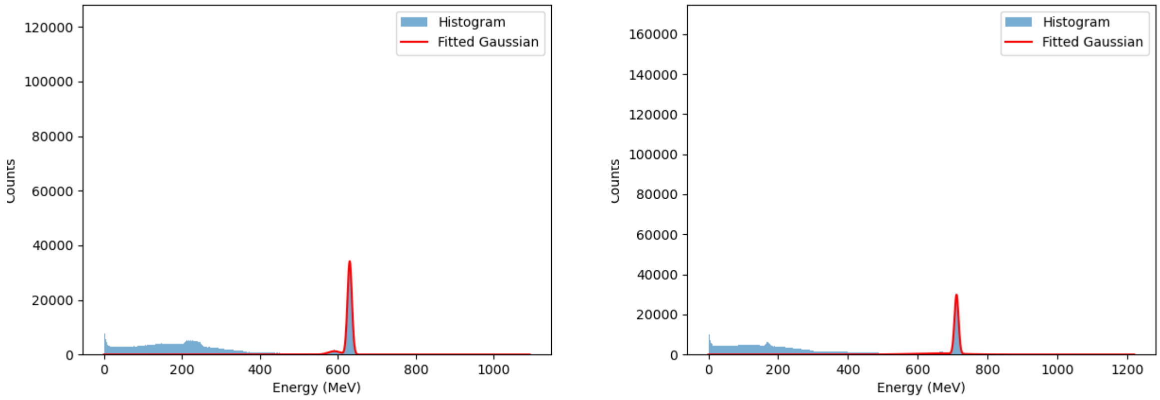

Figure 19: Helium-3 (1092 MeV) and Helium-4 (1220 MeV) Energy Profiles Before the Implementation of ΔE-E Filter

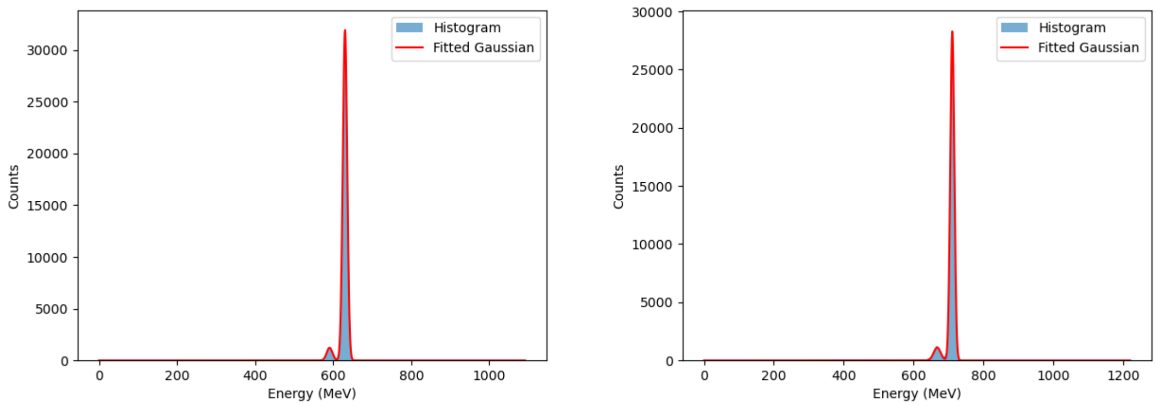

Figure 20: Helium-3 (1092 MeV) and Helium-4 (1220 MeV) Energy Profiles After the Implementation of ΔE-E Filter

The application of ΔE-E filter led to an overall increase in rejection rates, for both helium-3 and helium-4 ions. Helium-4 showed a more substantial increase in rejection rates compared to helium-3. Helium-4 benefits more from the application of the ΔE-E compared to helium-3. Helium-4's higher fragmentation rate, including fragmentation into helium-3, results in a more complex energy deposition profile, requiring more stringent filtering to reduce noise and improve image quality. In contrast, helium-3, with less fragmentation, experiences a smaller increase in rejection rates after filtering, indicating that while both ions benefit from the filter, helium-4 depends on it more significantly to maintain image clarity.

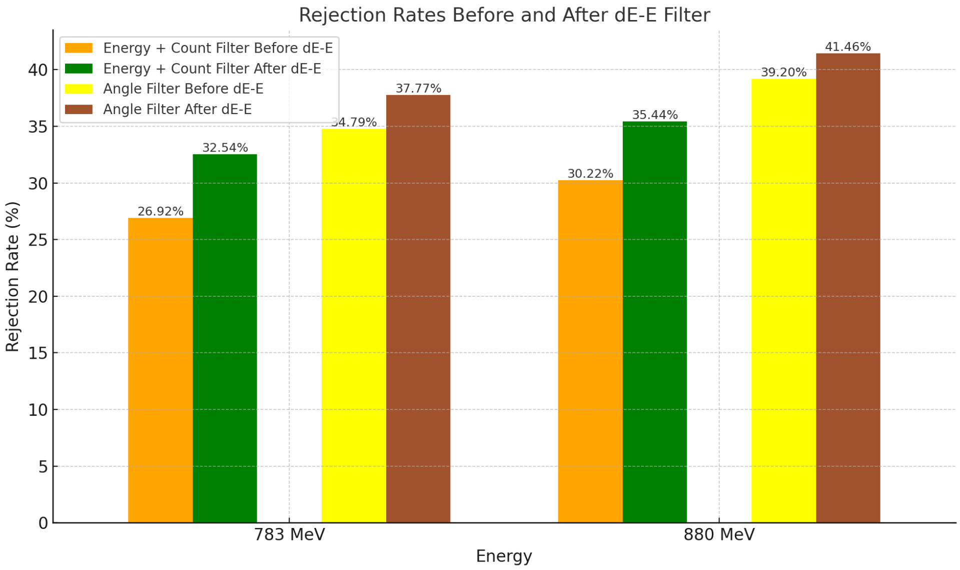

Figure 21: The Comparison of Rejection Rates at 32 cm Depth After Implementing ΔE-E Filter

The application of the ΔE-E filter has a noticeable impact on the resulting WEPL images. After implementing this filter, the images show a reduction in noise and clearer differentiation of the low contrast cylinders. Helium-4 shows slightly more uniformity in the WEPL distribution across the phantom at 32 cm depth, benefiting more from the filtering process.

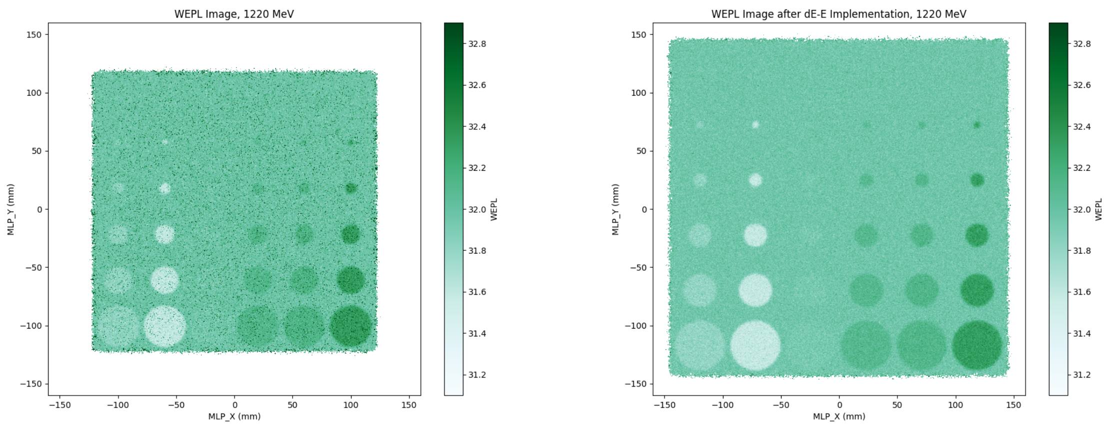

Figure 22: Reconstructed Images Before and After ΔE-E Filtration

3.5 Summary of simulation results

The results reveals that helium-3 and helium-4 ions perform similarly in radiographic imaging, with each ion showing strengths in different aspects. Helium-4 offers slightly better spatial resolution in smaller phantoms and provides superior contrast-to-noise ratio (CNR) at higher doses, especially in larger phantoms. Helium-3, however, excels in resolving finer details, particularly in low-contrast imaging, where it detects more structures with small contrast differences. In terms of Water Equivalent Path Length (WEPL) accuracy high contrast imaging, helium-3 shows better uniformity in larger phantoms, while helium-4 exhibits tighter accuracy in smaller setups, in low contrast imaging helium-3 exhibits higher accuracy at both depths. Both ion types benefit from the ΔE-E filter, which reduces noise and improves image clarity, though helium-4 requires more stringent filtering due to higher nuclear fragmentation.

4 Technical Integration Aspects

4.1 Synchrotron design

This study's simulation examined the ion energies potentially accelerated by the helium synchrotron developed by NIMMS. Engineered for high efficiency, the synchrotron was optimized to accelerate both helium ions and protons, incorporating a novel magnet design and an advanced injector LINAC. The technical specifications of the synchrotron are outlined below.

Table 10: Technical Specifications of the Compact Helium Synchrotron

Technical property	**Values**
Maximum magnetic rigidity	4.5 T/m
Maximum energy	220 MeV/u
Synchrotron circumference	33 m
Magnetic maximum field strength	1.65 T
RF frequency	352 MHz
Injection energy	5 MeV/u
Extraction methods	Slow and fast extraction
Helium ion source current	2 mA
Beam intensity	8×10^{10} ions per cycle
Maximum penetration depth	30 cm

The synchrotron provides both slow and fast extraction options and also supports mini-beam production, making it adaptable for imaging and treatment purposes. [1]

4.2 Beam properties

The relationship between the ion energy and RF frequency requires precise adjustments to the electric field at higher energy levels to maintain synchronization with the accelerating magnetic field. Due to the higher imaging energies required for helium-3, a higher RF frequency is necessary in the synchrotron design, based on the reference frequency of helium-4 as it is showed in figure 11.

Table 11: RF Frequencies for Helium-3 and Helium-4

Energy	783 MeV (He-3)	1092 MeV (He-3)	1220 MeV (He-4)	**220 MeV (He-4)**
RF Frequency	5.67 MHz	6.31 MHz	5.98 MHz	**5.34 MHz**

Single particle tracking approach limits beam current by the achievable detector read out rates.Additionally, based on a detector read-out rate of 1 MHz, based on literature review, the beam current is calculated to be approximately 3.20 nA, corresponding to a particle count of 1 million.

4.3 Detectors

While simulations are the foundation of this study, their clinical applications depend on the use of suitable detector technologies. These detectors are crucial for accurately tracking particle trajectories and measuring energy losses, enabling precise imaging.

In particle radiography systems, particle tracking detectors are crucial for monitoring the trajectories of particles as they pass through a phantom. These systems, often accompanied by energy or range detectors, help measure the residual energy of particles, ensuring precise tracking and energy measurement. Heavier ions like helium are favored in some applications due to their predictable paths and reduced scattering compared to other ions like carbon, making them viable for clinical use. Tracking detectors can be categorized into two types: individual systems that capture the trajectory and energy loss of each proton and integrative systems that measure proton flux over a broader area. Individual systems provide high-resolution data but are more complex, whereas integrative systems offer a broader measurement approach and are useful for calculating WEPL from dose profiles. [20]

In terms of energy and range detection, calorimeters measure the energy of protons by stopping them, allowing for an assessment of residual energy post-patient. However, these face challenges with thin phantoms due to energy resolution limitations, which can result in uncertainty in low-WEPL (Water Equivalent Path Length) measurements. [21] Range detectors, on the other hand, measure the proton stopping depth but are affected by range straggling, which introduces fluctuations in stopping depth, and by the thickness of detector layers, which can impact accuracy. [22]

Timepix detectors are used in helium radiography due to their high spatial resolution, flexibility, and ability to precisely track ion particles, making them ideal for medical imaging applications. Technically, Timepix detectors are hybrid pixel detectors that can measure both energy deposition and the time of arrival for individual particles at each pixel. This capability allows for the reconstruction of particle paths and detailed analysis of energy loss, which is critical for accurate imaging in helium ion radiography. [23]

4.4 Ion sources

In AiSHA (Advanced Ion Source for Hadrontherapy Applications) type ion sources - proposed by Compact Helium Synchrotron design, - the production of helium-4 and helium-3 would present specific challenges. [1] While helium-4, being naturally abundant, can be readily extracted from helium gas through standard plasma generation techniques, helium-3 production is more complex due to its rarity and specialized sourcing from nuclear reactors or other controlled processes. The ionization of helium-3 requires precise tuning of the plasma conditions, including pressure and magnetic confinement, to accommodate its lower mass and reduce issues such as beam scattering and instability. These factors demand highly efficient plasma confinement and extraction systems, tailored specifically for the unique dynamics of helium-3. [24]

5 Conclusions

Helium-3 shows strong potential for implementation in helium radiography due to several key advantages. Both ions achieved comparable image quality.

- **Spatial resolution**: Spatial resolution was assessed at both the 10 % and 50 % MTF levels. For the 16 cm phantom, helium-4 achieved 5% better resolution at the 10 % MTF level (2.099 cycles/mm for helium-4 vs. 1.995 cycles/mm for helium-3) and 4.7 % better at the 50% MTF level (1.019 cycles/mm for helium-4 vs. 0.971 cycles/mm for helium-3). However, for the 32 cm phantom, helium-3 outperformed helium-4 with an 11.9 % improvement at the 10 % MTF level (1.093 cycles/mm for helium-3 vs. 0.977 cycles/mm for helium-4) and 8.3 % better resolution at the 50 % MTF level (0.431 cycles/mm for helium-3 vs. 0.398 cycles/mm for helium-4).
- **General WEPL accuracy**: Helium-3 provided more uniform image reconstruction in larger phantoms, highlighting better accuracy for larger depths. Helium-4 demonstrated tighter accuracy in smaller setups, with fewer extreme pixel differences. In the low contrast phantom, helium-3 consistently performed better, with fewer large deviations from the theoretical model, particularly at greater depths.
- **CNR and dose efficiency**: In the 16 cm phantom, to achieve a CNR of 20, for example, helium-3 required approximately 1.2 times the dose needed for helium-4. In the 32 cm phantom, to achieve a

CNR of 20, helium-4 required 1.5 times the dose compared to helium-3. At higher doses, helium-4 demonstrated better CNR performance for larger phantom, while helium-3 - for smaller phantom.

– **Rejection rate**: Helium-3 exhibited consistently lower rejection rates, approximately 5-10 % lower than helium-4, suggesting that helium-3 may require less stringent filtering. This reflects reduced ion fragmentation and lower required imaging doses for helium-3, improving its practical viability in medical imaging.

One of the standout features of helium-3 is its lower fragmentation rate compared to helium-4. This not only leads to reduced noise but also minimizes the complexity of image filtering and data correction required to achieve clear, high-quality images. The reduced need for intense filtration processes like ΔE-E means that helium-3 can offer more straightforward and reliable image reconstruction, which is advantageous for practical implementation, such as a less complicated detector design.

Helium-3's ability to resolve finer details in low contrast environments suggests it is well-suited for medical imaging applications where subtle differences in density or composition are critical. This can have a significant impact on diagnostic imaging, where detecting small variations in tissue density is crucial for early detection of abnormalities.

The research suggests that helium-3 could be more effective for imaging at greater depths, which may make it a valuable tool in medical radiography for scanning larger body parts.

5.1 Challenges

– Real-Time imaging: The simulations were based on idealized, static models, however, in clinical practice, dynamic tracking is important for precise Bragg-peak localization and dose distribution. To fully leverage the potential of helium radiography, systems must be able to account for patients movement and anatomical changes in real time.

– Implementation and Scalability: Cost, systems compatibility and scalability must be considered to integrate this technology into routine clinical practice. The development of detector technologies and data acquisition systems is crucial for incorporating helium radiography in existing treatment infrastructures.

– Production of helium-3 ions: As helium-3 is rare and primarily sourced from nuclear reactors or the decay of tritium, making it expensive and difficult to obtain in large quantities. Additionally, the specialized infrastructure required for helium-3 production and storage further complicates its widespread implementation in radiography.

6 Bibliography

Bibliography

[1] Vretenar, M., et al.(2019). Conceptual design of a compact synchrotron-based facility for cancer therapy and biomedical research with helium and protons beams. *Journal of Physics: Conference Series*, 1255, 012018. doi:10.1088/1742-6596/1255/1/012018.

[2] Zhang, R., & Newhauser, W. D. (2009). The physics of proton therapy. Physics in Medicine and biology, 54(16), R193.

[3] Schneider, U., Pedroni, E., & Lomax, A. (1996). The calibration of CT Hounsfield units for radiotherapy treatment planning. Physics in Medicine and Biology, 41(1), 111-124.

[4] Schulte, R. W., Penfold, S. N., Tafas, J. T., & Schubert, K. E. (2008). A maximum likehood proton path formalism for application in proton computed tomography. Medical Physics, 35(11), 4849-4856

[5] Allison, J., et al. "Recent developments in GEANT4." Nuclear Instruments and Methods in Physics Research Section A: Accelerators, Spectrometers, Detectors and Associated Equipment 835 (2016): 186-225.

[6] Wellisch, J. P., & Hainzl, J. "Hadronic shower models in GEANT4." Nuclear Physics B - Proceedings Supplements 125 (2003): 60-63. DOI: 10.1016/S0920-5632(03)90994-1.

[7] Mokhov, N. V., & Striganov, S. I. "Simulation of hadronic showers." Fermilab-Conf-06-250-AD (2006).

[8] Apostolakis, J., et al. "GEANT4 physics processes for low energy neutron tracking: Improvements and performance." IEEE Transactions on Nuclear Science 53.6 (2006): 3469-3475.

[9] Napoli, M. D., Romano, F., D'Urso, D., et al. (2014). Nuclear reaction measurements on tissue-equivalent material and Geant4 Monte Carlo simulation for hadron therapy. Physics in Medicine & Biology, 59(24), 7643-7652.

[10] Cao, M., Deng, J., He, W., et al. (2023). Geant4 simulation of energy deposition ratio and physical processes of CdZnTe crystals irradiated by high energy particles. Applied Physics A, 129(595).

[11] Martisikova, M., Gehrke, T., Berke, S., Arico, G., & Jakel, O. (2018). Helium ion beam imaging for image guided ion radiotherapy. Radiation Oncology, 13(109), 1-15.

[12] Liu, H., Wng, S., & Xu, S. (2022). Longitudinal beam dynamic design of 500 kW beam power upgrade for CSNS-II RCS. Radiation Detection Technology and Methods, 6(3), 293-302.

[13] Voltz, L., et al. (2021). The accuracy of helium ion CT based particle therapy range prediction: an experimental study comparing different particle and x-ray CT modalities. Physics in Medicine and Biology, 66(2), 025003.

[14] Herman, M. G., et al. (2000). Guide to clinical use of electronic portal imaging. Journal of Applied Clinical Medical Physics, 1(2), 2645.

[15] https://geant4-userdoc.web.cern.ch/UsersGuides/ForApplicationDeveloper/html/Appendix/materialNames.html

[16] C. (2024). Focus stacking single-event particle radiography for high spatial resolution images and 3D feature localization. Physics in Medicine and Biology, 69(2), 025002. doi:10.1088/1361-6560/ad131a..

[17] Voltz, L., et al. (2020). Theoretical considerations on the spatial resolution limit of single-event particle radiography. Biomedical Physics & Engineering Express, 6(2), 025001.

[18] Schneider, U., et al. Methods for Modulation Transfer Function Calculation in Medical Imaging. Physics in Medicine and Biology, 2010.

[19] Rodríguez-Molares, et al.** (2020). The Generalized Contrast-to-Noise Ratio: A Formal Definition for Lesion Detectability. IEEE Transactions on Ultrasonics, Ferroelectrics, and Frequency Control, 67(5), 1001-1012.

[20] Sarosiek, et al. (2021). Analysis of characteristics of images acquired with a prototype clinical proton radiography system. Medical Physics, 48(6), 3071-3080.

[21] Muhuri, et al. (2014). Test and characterization of a prototype silicon–tungsten electromagnetic calorimeter. Nuclear Instruments and Methods in Physics Research Section A: Accelerators, Spectrometers, Detectors and Associated Equipment, 764, 1-6.

[22] Granja, et al. (2021). Wide-range tracking and LET-spectra of energetic light and heavy charged particles. Nuclear Instruments and Methods in Physics Research Section A: Accelerators, Spectrometers, Detectors and Associated Equipment, 987, 164901.

[23] Dudák, et al. (2018). Compact four-layer Timepix-based particle tracker WidePIX 3D: the first applications in X-ray CT imaging. Journal of Instrumentation, 13(12), C12001.

[24] Castro, A., et al. (2023). Experimental characterization of gaseous ion beams produced with the advanced ion source for hadrontherapy (AISHa) at 18 GHz. Review of Scientific Instruments, 94(5), 053301.